JACS
JOURNAL OF THE AMERICAN CHEMICAL SOCIETY
pubs.acs.org/JACS
Article

N and OH-Immobilized Cu_3 Clusters In Situ Reconstructed from Single-Metal Sites for Efficient CO_2 Electromethanation in Bicontinuous Mesochannels

Fuping Pan,* Lingzhe Fang,+ Boyang Li,+ Xiaoxuan Yang, Thomas O'Carroll, Haoyang Li, Tao Li,* Guofeng Wang,* Kai-Jie Chen,* and Gang Wu*

Cite This: J. Am. Chem. Soc. 2024, 146, 1423−1434
Read Online
ACCESS | Metrics & More | Article Recommendations | Supporting Information

Downloaded via UNIV OF PITTSBURGH on January 25, 2024 at 19:56:21 (UTC).
See https://pubs.acs.org/sharingguidelines for options on how to legitimately share published articles.

ABSTRACT: Cu-based catalysts hold promise for electrifying CO_2 to produce methane, an extensively used fuel. However, the activity and selectivity remain insufficient due to the lack of catalyst design principles to steer complex CO_2 reduction pathways. Herein, we develop a concept to design carbon-supported Cu catalysts by regulating Cu active sites' atomic-scale structures and engineering the carbon support's mesoscale architecture. This aims to provide a favorable local reaction microenvironment for a selective CO_2 reduction pathway to methane. In situ X-ray absorption and Raman spectroscopy analyses reveal the dynamic reconstruction of nitrogen and hydroxyl-immobilized Cu_3 ($N,OH\text{-}Cu_3$) clusters derived from atomically dispersed $Cu{-}N_3$ sites under realistic CO_2 reduction conditions. The $N,OH\text{-}Cu_3$ sites possess moderate *CO adsorption affinity and a low barrier for *CO hydrogenation, enabling intrinsically selective CO_2-to-CH_4 reduction compared to the C−C coupling with a high energy barrier. Importantly, a *block* copolymer-derived carbon fiber support with interconnected mesopores is constructed. The unique long-range mesochannels offer an H_2O-deficient microenvironment and prolong the transport path for the CO intermediate, which could suppress the hydrogen evolution reaction and favor deep CO_2 reduction toward methane formation. Thus, the newly developed catalyst consisting of in situ constructed $N,OH\text{-}Cu_3$ active sites embedded into bicontinuous carbon mesochannels achieved an unprecedented Faradaic efficiency of 74.2% for the CO_2 reduction to methane at an industry-level current density of 300 mA cm^{-2}. This work explores effective concepts for steering desirable reaction pathways in complex interfacial catalytic systems via modulating active site structures at the atomic level and engineering pore architectures of supports on the mesoscale to create favorable microenvironments.

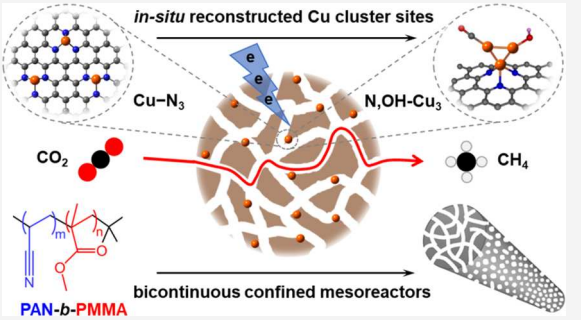

1. INTRODUCTION

Electrifying CO_2 transformation using renewable energy offers a carbon-neutral solution to CO_2 recycling and fuel generation.[1,2] Among various feedstocks from the CO_2 reduction reaction (CO_2RR), two electron-enabled CO and HCOOH have approached the performance thresholds for industry implementation.[3] Compared to lightly reduced products, deeply reduced products, such as hydrocarbons and oxygenates, are economically more attractive and hold significant market sizes.[1] Particularly, methane (CH_4), an extensively used fuel, is compatible with the existing storage and transportation infrastructure. Nevertheless, the current benchmarking performance of CO_2-to-CH_4 remains far below the applicable threshold owing to grand challenges associated with the complicated eight proton-coupled electron transfer (PCET) steps, adsorption/transformation of multiple carbonaceous intermediates, and competition with other reaction pathways beyond CH_4.[4−6] The success in achieving viable CO_2 electromethanation relies on the development of high-performance electrocatalysts.

Earth-abundant copper (Cu) is considered the most promising catalyst for reducing CO_2 to hydrocarbons; however, the CH_4 formation competes with C_2 products.[7,8] Modifying Cu by alloying and interfacial interaction can stabilize the *CHO intermediate and selectively produce CH_4 with suppressed C−C coupling on large-size Cu nanoparticles.[9,10] However, the current performance needs significant improvement to meet the needs of viable applications. Notably, single-atom Cu catalysts have shown great promise to steer reaction pathways in complex catalytic processes owing to their great designability of electronic properties.[5,11−14] To stabilize atomically dispersed metal sites,

Received: September 23, 2023
Revised: December 17, 2023
Accepted: December 18, 2023
Published: January 3, 2024

ACS Publications
© 2024 American Chemical Society

https://doi.org/10.1021/jacs.3c10524
J. Am. Chem. Soc. 2024, 146, 1423−1434

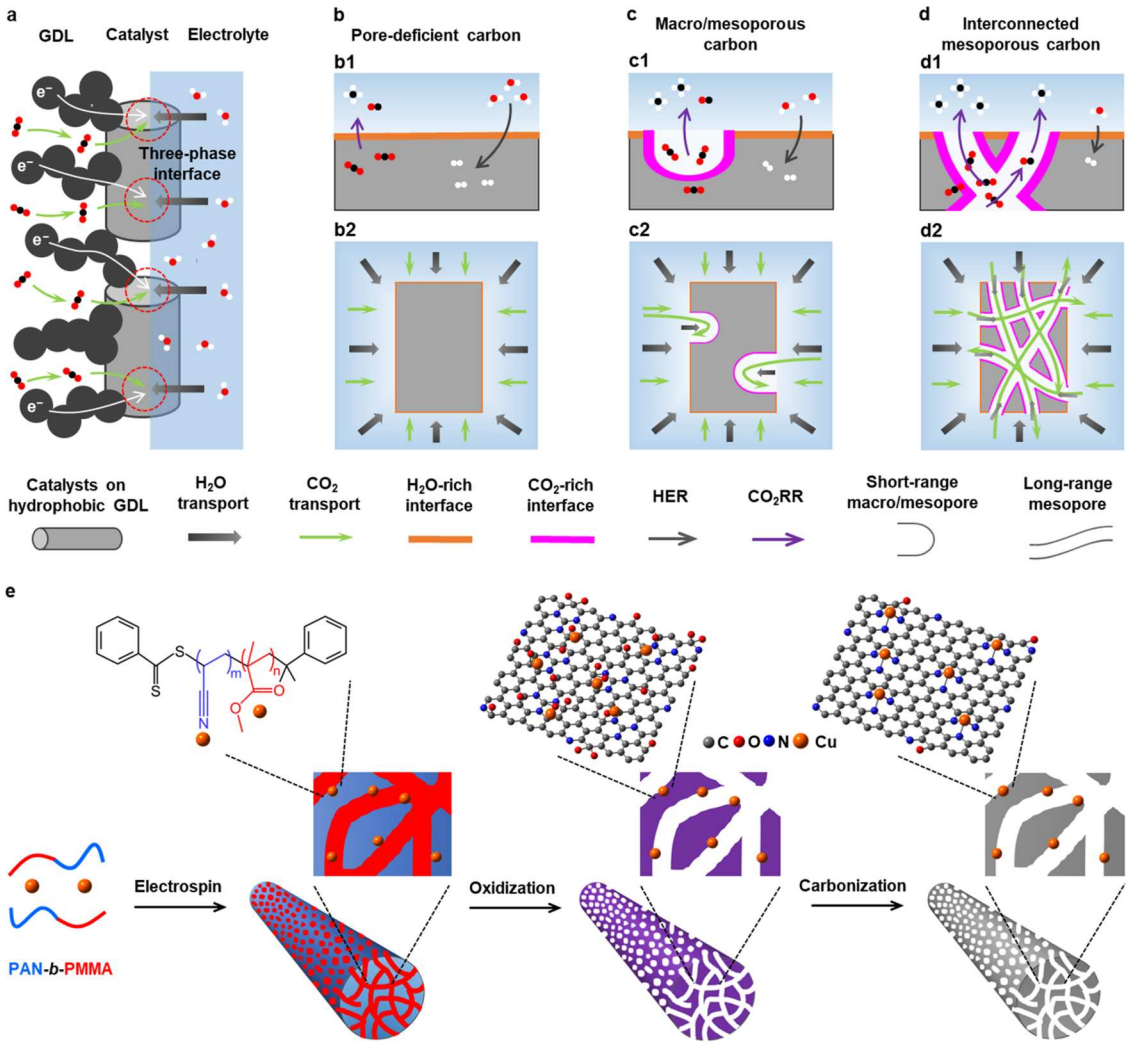

Figure 1. Design conception and catalyst synthesis. (a) Schematic showing the GDE structure. (b–d) CO_2RR/HER (b1, c1, and d1) and CO_2/H_2O transport (b2, c2, and d2) properties at the three-phase interface in the local reaction microenvironment of mesopore-deficient carbon (b), macro/mesoporous carbon (c), and interconnected mesoporous carbon supports (d). (e) Synthesis procedures for the Cu–N/IPCF derived from the PAN-*b*-PMMA *block* copolymer.

heteroatom-doped carbon supports, especially nitrogen-doped carbons, are desirable because of their remarkable tunability in their pore architecture, strong metal-heteroatom interaction, and enhanced electrochemical stability.[15−23] Several prior studies suggested that heteroatom-doped carbon-supported isolated Cu atoms are not electrochemically stable under negative potentials of realistic CO_2RR conditions and would likely be reduced to metallic Cu species, acting as the catalytic site for CO_2 reduction to CO, C_2H_4, and C_2H_5OH.[24−27] In situ reconstruction of single-atom Cu during CO_2-to-CH_4 conversion was reported on oxide-supported isolated Cu,[13] Cu-based metal–organic frameworks,[28] and undoped carbon nanotube-supported Cu-phthalocyanine molecular catalysts.[29] However, to our knowledge, such dynamic reconstruction of single-atom Cu has not been demonstrated yet on N-doped carbon supports in CH_4 generation. Hence, there is a need for an in-depth study of the potential-driven atomic-level structure reconstruction of N-doped carbon-supported single-atom Cu sites and their catalytic mechanisms toward CO_2-to-CH_4 reduction.

Apart from the atomic structure of carbon-supported Cu sites, the local reaction microenvironment also plays a critical role in CO_2 reduction, which is highly associated with the pore architecture of carbon supports.[17,30−32] To drive CO_2-to-CH_4 conversion, optimization of the CO_2/H_2O concentration and elongation of the transport path for CO intermediate are vital for suppressing the side hydrogen evolution reaction (HER) at large overpotentials where CH_4 formation occurs and promoting a deep CO reduction, respectively.[31,33] Challengingly, such expectations cannot be readily realized on conventional carbon supports with deficient and short-range pores due to the significant fraction of H_2O warping within the catalyst surface and the rapid loss of CO intermediates from the surface. We hypothesized that constructing bicontinuous mesoporous carbon to host Cu sites could create H_2O-deficient yet CO_2-rich surfaces to restrain the HER because H_2O penetration in the pore region of catalysts loaded on the hydrophobic gas diffusion layer (GDL) can be suppressed. Moreover, interconnected mesochannels would offer a long-range enhanced confinement space for increasing the residence time of the CO intermediate toward enabling effective interactive contact with Cu sites,[34,35] thereby creating a deep reduction-favorable local microenvironment.

https://doi.org/10.1021/jacs.3c10524
J. Am. Chem. Soc. 2024, 146, 1423−1434

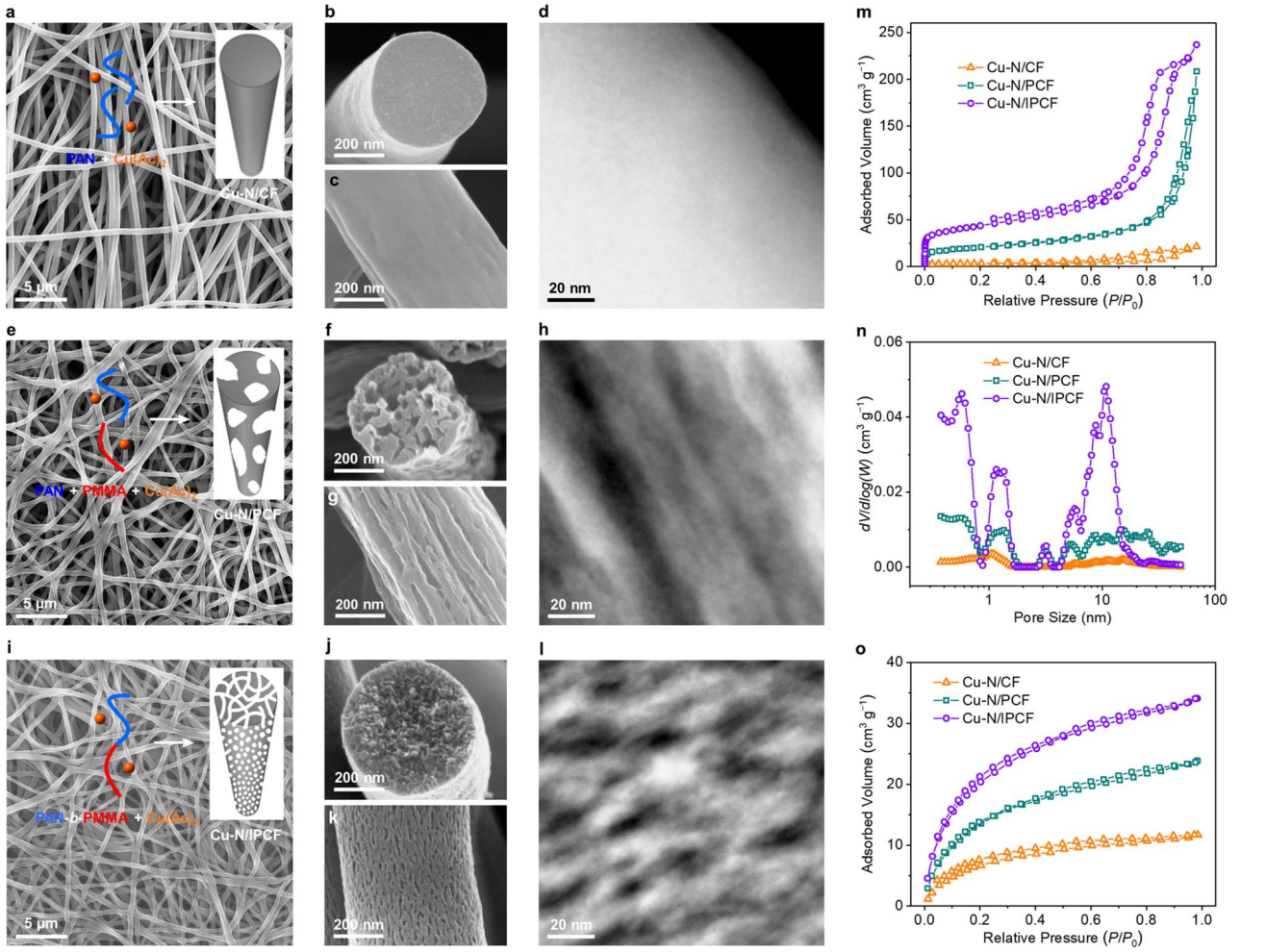

Figure 2. Characterization of the morphology and pore structure. SEM and STEM images of (a–d) Cu–N/CF, (e–h) Cu–N/PCF, and (i–l) Cu–N/IPCF. (m) N_2 gas adsorption–desorption isotherms, (n) pore size distribution, and (o) CO_2 adsorption–desorption isotherms for these catalysts. Inserts a–i show precursors used for synthesizing catalysts and the corresponding pore structure.

We sought to develop bicontinuous mesoporous carbon for supporting atomically dispersed Cu, aiming to engineer both active site structure and the local reaction microenvironment toward efficient CO_2-to-CH_4 conversion. To this end, we implemented the molecule-level microphase separation of a polyacrylonitrile-*block*-poly(methyl methacrylate) (PAN-*b*-PMMA) *block* copolymer to create interconnected mesoporous carbon fiber (IPCF) supports with abundant, uniform, and bicontinuous mesochannels for stabilizing isolated Cu–N_3 moieties (Cu–N/IPCF). More importantly, in situ X-ray absorption and Raman spectroscopy studies revealed the dynamic reconstruction of atomically dispersed Cu to nitrogen and hydroxyl-immobilized Cu_3 (N,OH-Cu_3) clusters during the operating CO_2 reduction conditions. They are the actual active sites to promote electrochemical CO_2-to-CH_4 reduction, as elucidated by extensive experimental analyses and theoretical calculations. Accordingly, the synergistic coupling of in situ formed N,OH-Cu_3 sites and bicontinuous confined mesoreactors effectively suppresses the HER. It steers selective CO_2 electromethanation, endowing the newly designed catalyst with significantly enhanced performance.

2. RESULTS AND DISCUSSION

2.1. Design and Synthesis of Catalysts. In CO_2 electrolysis at the gas–solid–liquid triple-phase boundary of the gas diffusion electrode (GDE) (Figure 1a), H_2O is required as a proton source for hydrocarbons. For carbon-supported Cu catalysts, H_2O is rich on the catalyst surface in the case of conventional pore-deficient carbon (Figure 1b) and short-range macro/mesoporous carbon supports (Figure 1c). At the same time, the CO_2 concentration is limited due to its low solubility and reaction with electrolytes particularly in alkaline conditions.[36,37] Such a CO_2-depleted and H_2O-rich interface results in the overwhelming HER at large overpotentials that are needed to drive a deep CO_2 reduction to CH_4.[33] To restrain the HER, we intended to design an IPCF support with suppressed H_2O penetration in the long-range mesopore region on the hydrophobic GDE, thus creating a large portion of the H_2O-deficient and CO_2-rich active interface (Figure 1d). A small amount of H_2O can still enter mesochannels along with the CO_2 stream, providing a proton source with suppressed HER competition. The long-range mesochannels could also promote CH_4 formation by confining CO intermediates in the mesochannel reactors to boost its successive reduction over the Cu sites;[34,35] such benefits are not inherently owned by conventional carbon supports with sparse and short-range macro/mesopores.

To experimentally synthesize the as-proposed Cu–N/IPCF, a *block* copolymer-assisted approach was developed via the electrospinning, oxidation, and pyrolysis of the PAN-*b*-PMMA

https://doi.org/10.1021/jacs.3c10524
J. Am. Chem. Soc. 2024, 146, 1423–1434

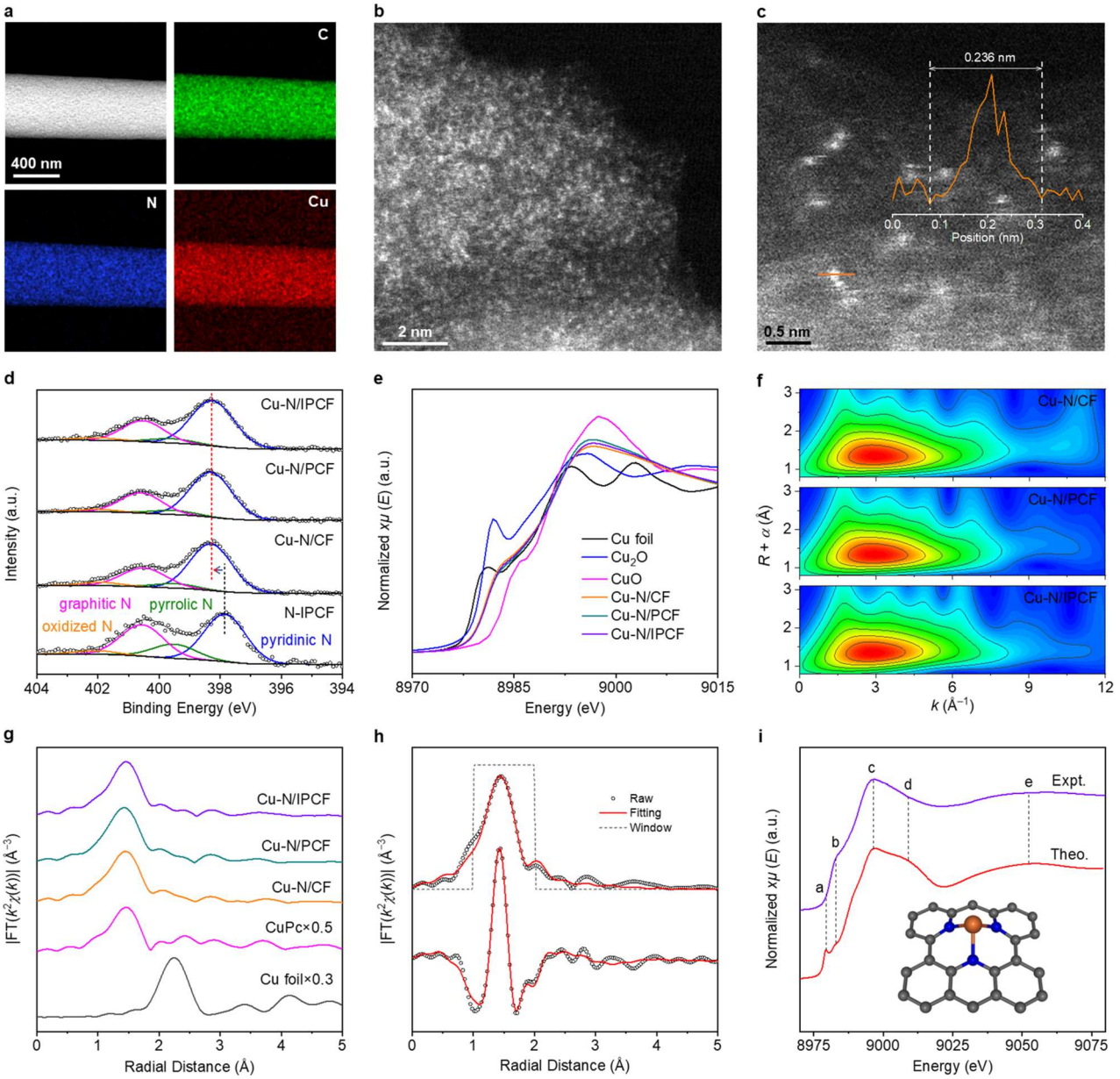

Figure 3. Atomic-level structural characterization of Cu. (a) Energy-dispersive spectroscopy elemental mapping and (b, c) HAADF-STEM images for Cu−N/IPCF. (d) N 1s XPS, (e) Cu K-edge XANES, (f) Wavelet transforms of EXAFS, (g) Fourier transforms of EXAFS spectra of catalysts and reference samples. (h) Fitting of the EXAFS spectrum for Cu−N/IPCF. (i) Comparison between the experimental Cu XANES spectrum and the theoretical spectrum of $Cu-N_3$.

polymer containing cupric acetate (Figure 1e and Figures S1 and S2). Due to the microphase separation of the PAN-*b*-PMMA, this approach allows for an accurate control over the evolution of continuous PMMA domain networks rooted in the PAN matrix at the molecular level.[38] It further navigates the generation of the IPCF support upon the removal of the PMMA template and atomically dispersed $Cu-N_3$ coordination by high-temperature thermal activation. The high homogeneity of single Cu sites enables us to probe their dynamic structure during the CO_2RR. We also synthesized another two types of catalysts as controls to justify the vital significance of bicontinuous mesopores. One is $Cu-N_3$ supported on a pore-deficient carbon fiber (Cu−N/CF) using PAN alone (Figure S3a), and the other is $Cu-N_3$ supported on a conventional porous carbon fiber with discontinuous macro/mesopores (Cu−N/PCF) using the physical PAN+PMMA blend (Figure S3b).

2.2. Morphology and Pore Structure of Catalysts. Owing to the absence of PMMA as pore templates, oxidizing Cu-PAN fibers and then transforming into the Cu−N/CF would not yield mesopores. This can be confirmed by scanning electron microscopy (SEM), transmission electron microscopy (TEM), and scanning transmission electron microscopy (STEM) images. The Cu−N/CF exhibited a fibrous morphology with a relatively smooth surface and no visible pores (Figure 2a−d and Figures S4−S7). In the Cu−N/PCF, the macrophase separation of the PAN and PMMA blend results in the formation of nonuniform and large PMMA domains over the PAN matrix, which act as pore-forming reagents and can be easily removed through oxidization at low temperatures in air. As a result, the Cu−N/PCF displayed

https://doi.org/10.1021/jacs.3c10524
J. Am. Chem. Soc. 2024, 146, 1423−1434

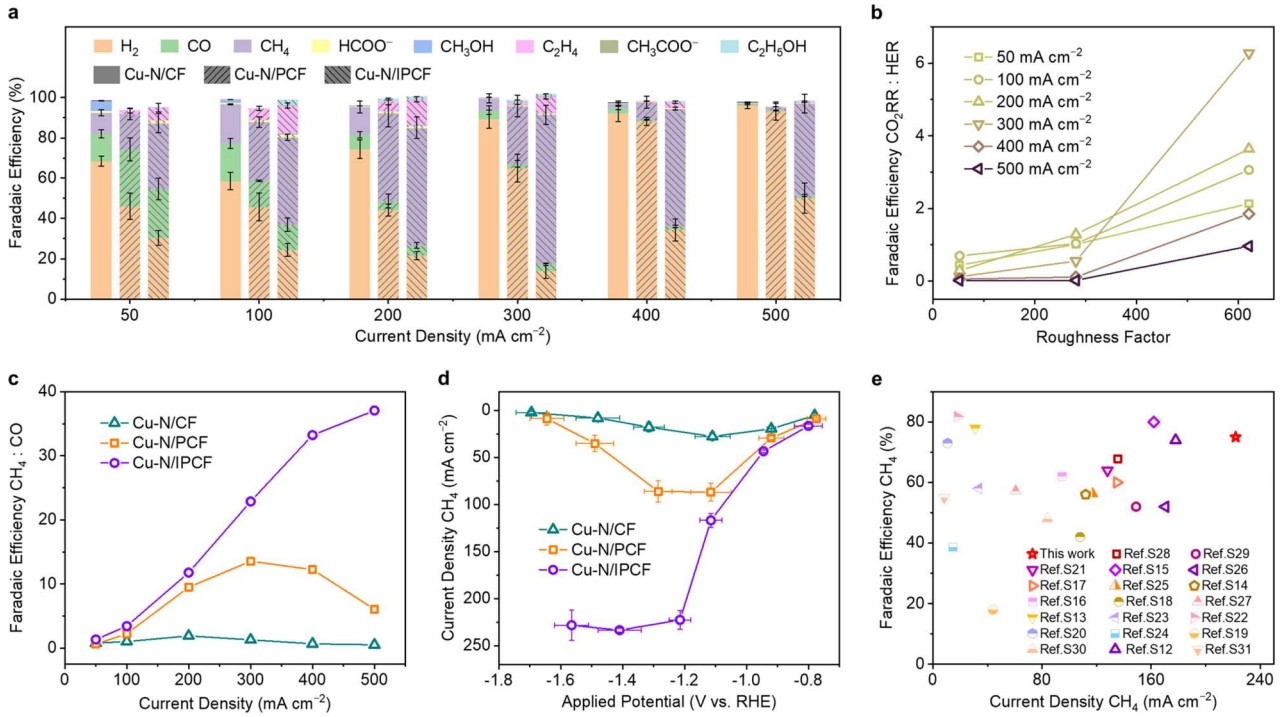

Figure 4. Electrochemical CO_2 reduction performance. (a) FEs of various products. (b) Correlation between RF and FE ratios of CO_2RR:HER. (c) FE ratios of CH_4:CO at various current densities for Cu−N/CF, Cu−N/PCF, and Cu−N/IPCF. (d) Partial current densities of CH_4 for Cu−N/CF, Cu−N/PCF, and Cu−N/IPCF. (e) Activity comparison between Cu−N/IPCF and typical Cu-based catalysts reported in the literature.

discontinuous and nonuniform macro/mesopores (Figure 2e−h). In contrast, the microphase separation of PAN-*b*-PMMA directs the generation of continuous and uniform PMMA domains in the PAN matrix,[38] thereby creating the unique IPCF for supporting isolated Cu atoms with dense and interconnected mesopores throughout the surface and cross-section (Figure 2i−l).

N_2 gas adsorption−desorption isotherm measurements further monitored the evolution of the different pore structures. The Cu−N/IPCF exhibited distinguishable features with pronounced type H1 hysteresis, confirming the existence of mesopores (Figure 2m), which was not observed with the Cu−N/CF and Cu−N/PCF samples. As for the pore size distribution, the Cu−N/IPCF showed a considerable number of mesopores with a narrow distribution centered at ∼9.3 nm (Figure 2n), whereas there are insignificant mesopores with a broad distribution in the Cu−N/PCF and fewer mesopores in the Cu−N/CF. Further, the Cu−N/IPCF displayed the largest surface area and CO_2 adsorption amount compared with the other two counterparts (Figure 2o and Table S1). These results validate the success in the synthesis of the rationally designed Cu−N/IPCF catalyst with uniform mesopores via the *block* copolymer-assisted method, prominently distinct from porosities of conventional Cu−N/PCP and Cu−N/CF prepared using a PAN+PMMA blend and PAN alone, respectively. The long-range mesopores could provide efficient CO_2 transport and prevent CO intermediates from quickly escaping due to the confined diffusion channels. The unique microenvironment favors the creation of CO_2-rich active surfaces and a desirable deep CO_2 reduction to CH_4.

2.3. Atomic-Level Structure of Single Cu Sites. We further elucidated the atomic-level structure of atomically dispersed Cu sites and their interaction with the carbon support. All catalysts showed a broad feature at ∼25° in X-ray diffraction (XRD) patterns (Figure S8), suggesting no Cu-containing crystalline species on the partially graphitized carbon support, in agreement with high-resolution TEM images and TEM diffraction patterns (Figure S9). Energy-dispersive spectroscopy elemental mapping images confirm the homogeneous distribution of Cu species in the N-doped carbon matrix (Figure 3a and Figure S10). The actual loadings of Cu in the three catalysts were determined to be approximately 11 wt % using inductively coupled plasma mass spectrometry (ICP-MS) (Table S1). The aberration-corrected high-angle annular dark-field scanning transmission electron microscopy (HAADF-STEM) images display dense bright spots with a size of ∼0.22 nm corresponding to isolated Cu atoms (Figure 3b,c and Figures S11 and S12). X-ray photoelectron spectroscopy (XPS) analyses show a high N content of ∼14.5 atom % in the surface layer of catalysts (Table S1). Deconvolution of the high-resolution N 1s spectra confirms the presence of pyridinic N (398.3 eV), pyrrolic N (400.1 eV), graphitic N (401.5 eV), and oxidized N (403.1 eV; Figure 3d). Compared to the Cu-free N-doped IPCF (N-IPCF), the position of pyridinic N shifted to a higher binding energy with an increased percentage over that of Cu-containing catalysts (Figure S13). In contrast, the position of other N species remained unchanged. This observation suggests that the stabilization of single Cu metals involves strong coordination with pyridinic N, forming Cu−N bonds due to the existence of lone-pair electrons on pyridinic N.[39−42]

The electronic states and local coordination of atomic Cu were further probed using Cu K-edge X-ray absorption spectroscopy (XAS). In the X-ray absorption near-edge spectroscopy (XANES), the edge positions of the three catalysts were located between the Cu_2O and CuO (Figure 3e and Figure S14). The Cu oxidation state was estimated at +1.25 based on the correlation between the oxidation state and

https://doi.org/10.1021/jacs.3c10524
J. Am. Chem. Soc. 2024, 146, 1423−1434

absorption edge position. The Cu 2p and LMM Auger spectra further confirm the presence of the Cu^+ species (Figure S15). The Fourier transform (FT) extended X-ray absorption fine structure (EXAFS) presents a notable peak at ~1.45 Å (Figure 3g), following the first Cu−N shell of the CuPc standard; no observable Cu−Cu bond at 2.35 Å (Cu foil) was detected. The Wavelet transform (WT) EXAFS analyses show only one maximum intensity at ~3.0 $Å^{-1}$ associated with the single-metal Cu−N pair without crystalline species (Figure 3f).[43,44] The fitting of EXAFS spectra unveils that the coordination number (CN) of Cu−N is 3.18−3.31 for these catalysts (Figure 3h, Figure S16, and Table S2), indicating that the isolated Cu is coordinated with approximately three pyridinic N atoms in the first shell forming a $Cu-N_3$ moiety. The precise atomic-level configuration was studied by comparing the experimental Cu K-edge XANES spectrum with the theoretical one simulated based on the FDMNES program. The simulated XANES result of the carbon-supported $Cu-N_3$ model fits the main features of the experimental XANES spectrum (Figure 3i), confirming the dominant $Cu-N_3$ structure in the as-prepared catalysts. The imperfect fitting is probably due to other minor structures as the high-loading metal amount (~11 wt %) may increase the nonuniformity of single-atom Cu sites.[45−47] The microscopic HAADF-STEM and spectroscopic XAS analyses unambiguously validate the well-defined, atomically dispersed, and N-coordinated $Cu-N_3$ sites at a high mass loading supported on three carbon supports.

2.4. Experimental Evaluation of CO_2 Reduction. In CO_2 electrolysis experiments, catalysts were deposited onto a hydrophobic GDL to increase the local concentration of gaseous CO_2 for achieving high current densities (Figure S17). CO_2 reduction performance was measured in a flow cell with an alkaline electrolyte under constant-current testing conditions. We detected four gaseous products (H_2, CO, CH_4, and C_2H_4) and four liquid-phase products ($HCOO^-$, CH_3OH, C_2H_5OH, and CH_3COO^-) from direct CO_2 reduction based on the $^{13}CO_2$ isotope labeling experiment (Figures S18−S20). Among them, $HCOO^-$ exhibits a significantly lower Faradaic efficiency (FE; <2%) than others. This can be attributed to the enhanced reactivity of the Cu site to form C-bonded *COOH rather than the O-bonded *OOCH intermediate. The former drives CO production and deep CO reduction to CH_4 and C_2 products through hydrogenation and C−C coupling, whereas the latter produces $HCOO^-$ as the final product.[48−50] Figure 4a shows FEs at current densities from 50 to 500 mA cm^{-2}. The Cu−N/CF achieved a maximum overall CO2RR FE of 40.6% at 100 mA cm^{-2}, which decreases drastically at larger current densities with significantly increased FEs for the HER. On the contrary, the HER was effectively suppressed on porous catalysts with remarkably increased CO_2RR:HER FE ratios (Figure S21), achieving the highest overall CO_2RR FE of 55.2% at 200 mA cm^{-2} on the Cu−N/PCF and 87.8% at 300 mA cm^{-2} on the Cu−N/IPCF catalyst.

The inhibition of the HER can be attributed to the highly porous structure. In a previous study, Surendranath et al.[51] demonstrated the mesostructure-induced transport limitations in the HER suppression on porous electrodes, which can be quantified using the roughness factor (RF). We calculated the RFs of our catalysts by normalizing the electrochemically active surface area of carbon support to the geometric area of the electrode (Figure S22 and S23), showing 53.3, 280.5, and 621.2 for the Cu−N/CF, Cu−N/PCF, and Cu−N/IPCF, respectively. We noted that the increase in RFs leads to an enhancement in the FE ratios of CO_2RR:HER (Figure 4b) along with tendencies of an increase in the CO_2RR current density (Figure S24), suggesting a strong dependence on CO_2 reduction on the porous structure of the electrode. Specifically, compared to the H_2O-rich surface on the less-porous Cu−N/CF, the porous Cu−N/PCF catalyst provides diffusion channels to deliver CO_2 to the catalyst surface within pores. At the same time, H_2O penetration is inhibited due to the hydrophobic nature of the GDE (Figure 1c). Such a mass transport gradient can be substantially enhanced on the Cu−N/IPCF because of its denser long-range mesopores (Figure 1d), building a CO_2-rich yet H_2O-depleted environment and enabling efficient CO_2 reduction at large currents.

We then analyzed the catalytic selectivity and activity of the CO_2 reduction. CO and CH_4 are the main products of these Cu-containing catalysts. In contrast, there are only trace amounts of CO_2RR-derived products on the Cu-free N-IPCF (Figure S25), verifying the highly active nature of Cu species toward CO_2 reduction. Calculating the FE ratio of CH_4:CO suggests that *block* copolymer-derived mesopores are essential for promoting deep CO transformation to CH_4 with the trend following the order of Cu−N/IPCF > Cu−N/PCF > Cu−N/CF, particularly at high current densities (Figure 4c). This observation can be ascribed to the steric nanoconfinement effect that enrich the *CO intermediate within bicontinuous mesopores.[34,35,52] This can be corroborated by in situ Raman spectroscopy (Figure S26), in which the bands at 286 and 382 cm^{-1} correspond to the frustrated rotation of adsorbed *CO and Cu−*CO stretching, respectively.[53,54] The surface-absorbed *CO appeared on the Cu−N/IPCF upon applying potentials negative than −1.0 V, which was not observed on Cu−N/PCF and Cu−N/CF. Therefore, compared to the Cu−N/CF and Cu−N/PCF, the Cu−N/IPCF could afford the most enhanced nanoconfinement contribution to prevent CO intermediates from escaping long-range mesochannels, considerably improving its residence time and successive reduction to CH_4 on the Cu sites before becoming gaseous CO (Figure 1b−d). Note that, although such a local CO-rich characteristic also contributes to the improvement in FE ratios of C_2:C_1 on the Cu−N/IPCF (Figure S27), the intrinsically higher CO_2-to-CH_4 reactivity than C−C coupling on the in situ reconstructed Cu site guarantees the enhanced selectivity of CH_4 compared to C_2 products. It is further discussed in the following in situ XAS studies and theoretical calculations.

A maximum CH_4 FE of 74.2% was achieved on the Cu−N/IPCF catalyst at −1.21 V, much higher than 43.4% on the Cu−N/PCF and 19.5% on the Cu−N/CF at −1.11 V. In addition, the Cu−N/IPCF exhibited a significantly larger partial current density than the Cu−N/CF and Cu−N/PCF at applied potentials negative than −1.11 V (Figure 4d) due to the inhibition in the HER rate. As a result, high-efficient CH_4 generation yields a partial current density of 222.6 mA cm^{-2} at −1.21 V. Remarkably, the performance of the Cu−N/IPCF places it at the top level among reported Cu-based catalysts (Figure 4e and Table S3), while performance improvement is still required to meet the profitable electricity-powered CO_2-to-CH_4 conversion.[55] The catalyst can maintain durable CO_2-to-CH_4 electrolysis at 300 mA cm^{-2} for 3 h (Figure S28a). However, a slight decrease in the CH_4 FE after 2 h is likely a consequence of the declined surface hydrophobicity of the GDE (Figure S28b).

https://doi.org/10.1021/jacs.3c10524
J. Am. Chem. Soc. 2024, 146, 1423−1434

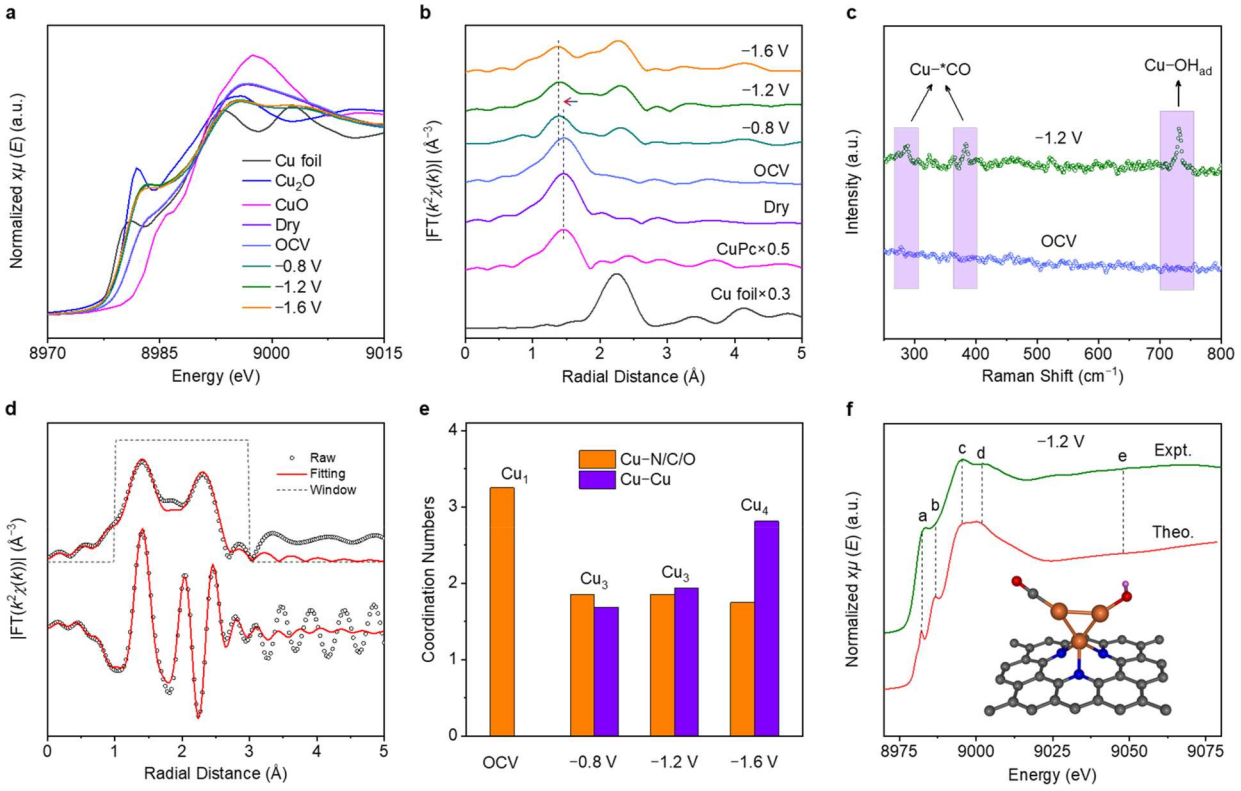

Figure 5. Identification of the active site structure by in situ characterizations. (a) In situ Cu K-edge XANES, (b) EXAFS, and (c) Raman spectra of the Cu−N/IPCF. (d) Fitting of the EXAFS spectrum obtained at −1.2 V. (e) Fitted CNs for Cu−N/C/O and Cu−Cu coordination at different potentials. (f) Comparison between the experimental Cu XANES spectrum at −1.2 V and the theoretical spectrum of the Cu_3−N_3−CO_1−OH_1 model. The brown, gray, blue, red, and pink spheres represent Cu, C, N, and H atoms, respectively.

2.5. Atomic-Level Cu Site Structure under Operating CO_2RR Conditions. To understand the actual active site structures, we performed in situ XAS to investigate the possible structure evolution of single Cu metal sites in the optimal Cu−N/IPCF catalyst under the operating CO_2 reduction conditions. The oxidation state of Cu remained unchanged under open-circuit voltage (OCV) and dry conditions based on XANES spectra (Figure 5a) and first-derivative profiles (Figure S29). However, it decreased from +1.25 to +1.06 when a negative potential of −0.8 V was applied. A further sweeping potential from −1.2 to −1.6 V resulted in the continuous reduction to +0.89. These results reveal the unstable characteristics of atomically dispersed Cu sites and the occurrence of electrochemical $Cu^{\delta+}$ reduction during the CO_2RR.

We continued exploring Cu structures by analyzing EXAFS spectra under dynamic electrochemical potentials. Like the fresh catalyst, no Cu−Cu coordination was observed under the OCV (Figure 5b). At −0.8 V, the Cu−Cu bond appeared at 2.28 Å, decreasing the Cu−N intensity relative to that at the OCV. Such transformations became intensified from −1.2 to −1.6 V, confirming the collapse of Cu−N_3 moieties and their dynamic reconstruction to metallic Cu species during the CO_2 reduction. Notably, the radial distance of Cu−N coordination under the realistic CO_2 reduction conditions declined by 0.07 Å compared to that at the OCV. The observation suggests the change in the first-shell coordination atoms toward Cu. Generally, the first-shell coordination of Cu are likely anchoring atoms from the carbon support, intermediates from the CO_2RR, and adsorbed species from the KOH electrolyte. In the N-doped carbon, N dopants possessing electron-withdrawing properties have a stronger interaction with metal than C atoms.[56] Thus, N dopants on the IPCF support might be the preferable anchoring sites to immobilize in situ formed metallic Cu species via a Cu−N interaction as also manifested by recent theoretical calculations.[26] The presence of adsorbed *CO intermediate and OH_{ad} groups can be confirmed by the in situ Raman spectrum (Figure 5c),[57,58] in which the *CO is from the CO_2 reduction and the OH_{ad} can be ascribed to the specific adsorption of weakly solvated OH^- ions from the electrolyte. The findings highlight the necessity of considering electrolyte properties in revealing site reconstruction. The decreased average bond length of Cu−N might be resulted from adding Cu−*CO and Cu−OH_{ad} bonding, generating Cu−N/C/O coordination over the metallic Cu species.

EXAFS spectra were further fitted to resolve the local coordination structures. As the first-shell coordinated N/C/O atoms in the fitting cannot be distinguished, Cu−N and Cu−Cu paths were included in the EXAFS fitting using Cu as the core (Figure 5d, Figure S30, and Table S4). The CNs of Cu−N is 3.25 at the OCV (Figure 5e), implying that Cu−N_3 remained stable in the CO_2-saturated electrolyte before the CO_2RR. Notably, the CNs changed drastically upon applying the CO_2 reduction potentials, showing 1.87/1.68, 1.85/1.94, and 1.75/2.81 for Cu−N/C/O and Cu−Cu at −0.8, − 1.2, and −1.6 V, respectively. The results suggest that single-atom Cu metals were transformed into the Cu_3 cluster at −0.8 and −1.2 V, which turned into the Cu_4 cluster with the potential down to −1.6 V. We further performed XANES simulations to reveal the atomic-level structure of Cu_3 at −1.2 V where the best CO_2-to-CH_4 performance was achieved. Given the

https://doi.org/10.1021/jacs.3c10524
J. Am. Chem. Soc. 2024, 146, 1423−1434

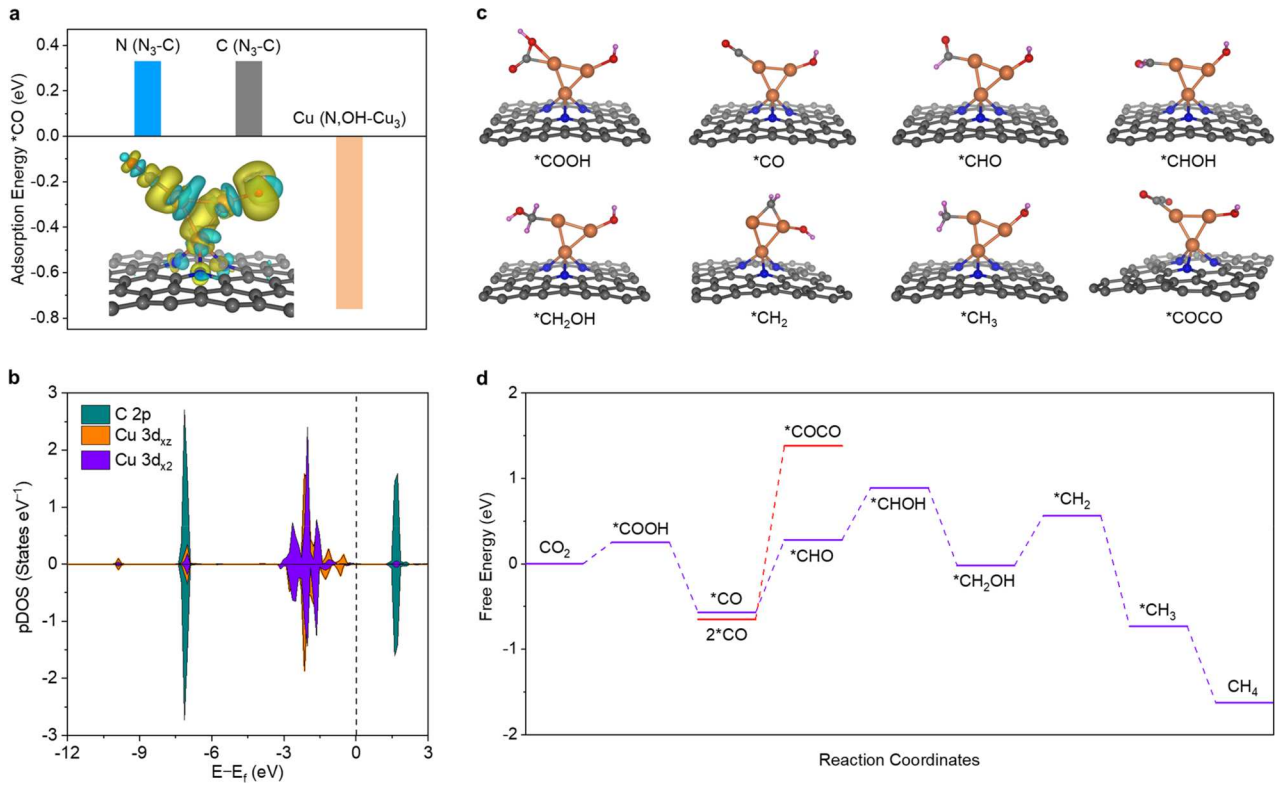

Figure 6. DFT calculations. (a) Predicated adsorption energy of *CO adsorbed on various sites. The inset is the charge density difference analysis of *CO on the N,OH-Cu_3. The yellow zone indicates the charge density increasing, and the cyan zone indicates the charge density decreasing. (b) Calculated density of states showing the orbital interaction between C 2p of *CO and Cu $3d_{xz}/d_{z2}$ of the N,OH-Cu_3. (c) Optimized adsorption configurations of various intermediates on the N,OH-Cu_3. (d) Free energy diagram of CO_2-to-CH_4 reduction and *COCO coupling on the N,OH-Cu_3 at U = 0 V vs RHE. The brown, gray, blue, red, and pink balls represent Cu, C, N, O, and H atoms, respectively.

configuration of N dopants, the adsorption of *CO/OH_{ad}, and the fitted CN for Cu−N/C/O, three possible structures were considered, including Cu_3−N_3-CO_1−OH_1, Cu_3−N_3-$(CO)_2$−OH_1, and Cu_3−N_3-CO_1−OH_2 (Figure 5f and Figure S31). Among them, the calculated XANES spectrum of the Cu_3−N_3-CO_1−OH_1 shows the best match with the experimental spectrum at −1.2 V than others, suggesting that the Cu_3−N_3−CO_1−OH_1 might be the dominant configuration derived from the in situ reconstruction of Cu−N_3 under CO_2 reduction at −1.2 V. The theoretical CN of Cu−N/C/O over the Cu_3−N_3−OH_1−CO_1 is 1.67, close to the fitted value of 1.85 in EXAFS. The structure also agrees with the fact that the oxidation state of electrochemically reduced Cu species is not zero due to a strong electron transfer from the metallic Cu_3 cluster to surrounding N-doped carbon, *CO intermediates, and adsorbed OH_{ad} species, leaving cationic Cu moieties. However, the theoretical XANES spectrum of the best-matching model shows a minor discrepancy compared with the experimental one. A similar phenomenon was observed on an Ag-supported Cu cluster[59] and an Fe−phthalocyanine molecular catalyst with a well-known structure.[60] This is probably due to H_2O molecules surrounding the active site, which may alter spatial coordinates of adsorbed species (e.g., *CO, OH_{ad}) through a hydrogen-bonding interaction at the catalytic solid−liquid interface, compared to those optimized by DFT calculations in vacuum conditions. In practice, extensive efforts still need to develop advanced experimental characterization and theoretical simulation methods for revealing the atomic-level structures of single-atom metals and their derivative sites under working conditions.

The similar reconstruction of single-atom Cu under operating CO_2 reduction conditions was elucidated in the literature. The in situ formed sites include subnanometric Cu_x (x: 2, 3, or 4) clusters[24−26] and nanoparticles with a size of ∼2−4 nm.[29,61] In contrast, many works demonstrated that carbon-supported single-atom Cu sites are electrochemically stable during the CO_2 reduction even at a negative potential of −1.6 V.[62−64] The variance is probably due to the difference in local coordination of the single-atom Cu and supports' structure/compositions of those reported catalysts, thus leading to different single-atom Cu−support interactions that mainly determine the electrochemical stability of the single-atom Cu center. In our case, single-atom Cu was converted into a Cu_3/Cu_4 cluster at −0.8 to −1.6 V rather than larger nanoparticles. This can be attributed to the strong stabilization effects from anchoring N dopants of the carbon support, *CO intermediate, and surface-adsorbed OH_{ad} groups. The strong interaction between these species and Cu atom clusters can reduce the surface energy of the Cu cluster and facilitate its formation as supported by the calculated formation energy (Figure S32). We have also characterized the spent catalyst by ex situ methods, displaying the single atomic characteristics of Cu species (Figures S33 and S34). The observation suggests the reversion of in situ formed Cu_3 clusters back to isolated Cu in the absence of an electric field and/or being exposed to air, which is in agreement with previous experimental and computational results.[24,25,65] Hence, N,OH-Cu_3 clusters, instead of atomically dispersed Cu−N_3, serve as the highly catalytic sites for the reduction of CO_2 to CH_4 at −1.2 V.

https://doi.org/10.1021/jacs.3c10524
J. Am. Chem. Soc. 2024, 146, 1423−1434

2.6. Theoretical Understanding of Catalytic Mechanisms. Density functional theory (DFT) calculations were performed to provide mechanistic insights. The N,OH-Cu_3 site determined from in situ XAS and Raman spectroscopy analyses was used as the model structure. In the CO_2-to-CH_4 transformation, the hydrogenation of *CO to *CHO is a key step,[4,64,66,67] which requires a relatively strong *CO adsorption to inhibit its desorption becoming gaseous CO. We first considered CO adsorption affinity on the Cu atom of the N,OH-Cu_3 and C/N atoms of the N_3−C (Figure 6a and Figure S35). The Cu site shows a negative adsorption energy of −0.76 eV, indicating favorable CO adsorption. However, positive adsorption energy suggests weak *CO binding on the N_3−C sites. This prediction suggests that the Cu atom of N,OH-Cu_3 is likely the catalytically active site for reducing CO_2 to CH_4 because its preferential *CO adsorption ensures deep *CO transformation. Charge-density analysis displays a strong electronic interaction between the *CO and N,OH-Cu_3 with electrons transferred from the Cu atom to *CO (insert of Figure 6a), enabling stable *CO binding and subsequent PCET-driven reduction to CH_4 on the N,OH-Cu_3 site. We further carried out a density-of-states (DOS) analysis to unveil the bonding interaction upon the adsorption of *CO on the N,OH-Cu_3. The Cu $3d_{xz}/d_{x2}$ orbitals participate in orbital coupling with C 2p of the *CO adsorbate based on their orbital overlapping (Figure 6b and Figure S36).

We further calculated the free-energy diagram. The elemental pathways involving *COOH, *CO, *CHO, *CHOH, *CH_2OH, *CH_2, and *CH_3 intermediates were considered,[64,68,69] of which the most critical *CO intermediate was manifested by in situ Raman (Figure 5c). The adsorption configurations of the C-bound intermediates are depicted in Figure 6c. The results show that free energy barriers are 0.25, 0.85, 0.61, and 0.58 eV for the activation of CO_2 to *COOH, hydrogenation of *CO to *CHO, transformation of *CHO to *CHOH, and reduction of *CH_2OH to *CH_2 on the N,OH-Cu_3 (Figure 6d), respectively. The other elementary steps are thermodynamically downhill. Thus, the hydrogenation of *CO to *CHO is the potential-limiting step in reducing CO_2 to CH_4. During the CO_2 reduction, C−C coupling is a grand obstacle toward selective CH_4 production. Here, the free-energy barrier for *CO dimerization, a key step to forming a C−C bond,[70−72] was calculated to be 2.03 eV. This value is significantly larger than that of the CH_4 formation. The results reveal the intrinsically enhanced capability in steering improved CO_2-to-CH_4 selectivity with the suppressed C_2 pathway on the N,OH-Cu_3 site. The promoting role of surface-bound OH_{ad} species in CH_4 generation was also verified based on the increased free energy barrier for *CO hydrogenation on OH_{ad}-free N−Cu_3 compared to that on N,OH-Cu_3 (Figure S37). Hence, the theoretical predictions support the experimentally enhanced CO_2-to-CH_4 activity of the in situ formed N,OH-Cu_3 clusters derived from monodispersed Cu−N_3 moieties under realistic CO_2RR conditions.

3. CONCLUSIONS

In summary, this study demonstrated a catalyst design principle of integrating atomic-level tuning of the Cu site's structure with mesoscale engineering of the carbon support's pore architecture, aiming to steer the CO_2 reduction to CH_4. The combined experimental and theoretical investigations validated the effectiveness of this strategy toward CO_2-to-CH_4 conversion on the carbon-supported Cu catalysts consisting of in situ constructed N and OH-immobilized Cu_3 clusters embedded into bicontinuous carbon mesochannels.

Utilizing the microphase separation of a PAN-*b*-PMMA *block* copolymer, a long-range interconnected mesoporous N-doped carbon fiber support was constructed to host atomically dispersed and N-coordinated Cu moieties. The carbon support with bicontinuous mesochannels provides a favorable local reaction microenvironment, which offers H_2O-deficient and CO_2-rich interfaces in the pore region while suppressing the hydrogen evolution reaction. Also, it creates an enhanced nanoconfinement space with an extended transport path for the CO intermediate, facilitating deep CO_2 reduction to methane. More importantly, in situ electrochemical XAS and Raman spectroscopy analyses revealed a unique dynamic reconstruction of atomically dispersed Cu sites to Cu_3 clusters immobilized by nitrogen of the carbon support and hydroxyl species from the electrolyte under the operating CO_2 reduction conditions. The in situ constructed Cu_3 species is the actual catalytic site for efficient CO_2-to-CH_4 reduction. DFT calculations further predicted that the N and OH-stabilized Cu_3 clusters selectively drive the CH_4 formation with the suppressed C_2 pathway along an energetically favored CO_2 → *CO → *CHO → *CH_2OH → CH_4 route.

The synergy of in situ formed N,OH-Cu_3 sites and long-range confined mesoreactors benefits the CO_2-to-CH_4 conversion with a Faradaic efficiency of 74.2% at an industry-level current density of 300 mA cm^{-2}. This work holds great promise for practical CO_2-to-fuel electrolysis implementation. The rational catalyst design principles could create an effective platform for building advanced catalysts with optimal structures at a multiscale capable of regulating reaction pathways and selectivity for complex catalytic reactions associated with multiple elemental steps and intermediates.

■ ASSOCIATED CONTENT

Supporting Information

The Supporting Information is available free of charge at https://pubs.acs.org/doi/10.1021/jacs.3c10524.

Experimental details, additional characterization, electrochemical performance, and DFT data (PDF)

■ AUTHOR INFORMATION

Corresponding Authors

Fuping Pan − *School of Chemistry and Chemical Engineering, Northwestern Polytechnical University, Xi'an, Shaanxi 710072, China; Chongqing Innovation Center, Northwestern Polytechnical University, Chongqing 401135, China*; Email: fupingpan@nwpu.edu.cn

Tao Li − *Chemistry and Material Science Group, X-ray Science Division, Argonne National Laboratory, Lemont, Illinois 60439, United States; Department of Chemistry and Biochemistry, Northern Illinois University, DeKalb, Illinois 60115, United States*; Email: taoli@aps.anl.gov

Guofeng Wang − *Department of Mechanical Engineering and Materials Science, University of Pittsburgh, Pittsburgh, Pennsylvania 15261, United States*; Email: guw8@pitt.edu

Kai-Jie Chen − *School of Chemistry and Chemical Engineering, Northwestern Polytechnical University, Xi'an, Shaanxi 710072, China*; Email: ckjiscon@nwpu.edu.cn

Gang Wu − *Department of Chemical and Biological Engineering, University at Buffalo, The State University of*

https://doi.org/10.1021/jacs.3c10524
J. Am. Chem. Soc. 2024, 146, 1423−1434

New York, Buffalo, New York 14260, United States; Email: gangwu@buffalo.edu

Authors

Lingzhe Fang − *Department of Chemistry and Biochemistry, Northern Illinois University, DeKalb, Illinois 60115, United States*

Boyang Li − *Department of Mechanical Engineering and Materials Science, University of Pittsburgh, Pittsburgh, Pennsylvania 15261, United States*

Xiaoxuan Yang − *Department of Chemical and Biological Engineering, University at Buffalo, The State University of New York, Buffalo, New York 14260, United States*

Thomas O'Carroll − *Department of Chemical and Biological Engineering, University at Buffalo, The State University of New York, Buffalo, New York 14260, United States*

Haoyang Li − *School of Chemistry and Chemical Engineering, Northwestern Polytechnical University, Xi'an, Shaanxi 710072, China*

Complete contact information is available at: https://pubs.acs.org/10.1021/jacs.3c10524

Author Contributions

[+]F.P., L.F., and B.L. contributed equally. The manuscript was written through the contributions of all authors.

Notes

The authors declare no competing financial interest.

■ ACKNOWLEDGMENTS

F.P. acknowledges the support from the National Natural Science Foundation of China (no. 22309146), the Natural Science Foundation of Chongqing, China (no. CSTB2023NSCQ-MSX0429), and Fundamental Research Funds for the Central Universities. F.P. thanks Prof. Guoliang Liu at Virginia Tech for valuable discussion on the synthesis of the N-IPCF. K.-J.C. appreciates the support from the National Natural Science Foundation of China (no. 22071195) and The Youth Innovation Team of Shaanxi Universities. G.Wang acknowledges the support from the U.S. National Science Foundation (nos. CBET-1804326 and DMR 1905572). This research used resources of the Advanced Photon Source, a U.S. Department of Energy (DOE) Office of Science User Facility operated for the DOE Office of Science by Argonne National Laboratory under contract no. AC02-06CH11357. G.Wu appreciates the partial support from U.S. National Science Foundation (no. CBET-2223467).

■ REFERENCES

(1) De Luna, P.; Hahn, C.; Higgins, D.; Jaffer, S. A.; Jaramillo, T. F.; Sargent, E. H. What would it take for renewably powered electrosynthesis to displace petrochemical processes? *Science* **2019**, *364*, 3506.

(2) Yang, Y.; Louisia, S.; Yu, S.; Jin, J.; Roh, I.; Chen, C.; Fonseca Guzman, M. V.; Feijóo, J.; Chen, P.-C.; Wang, H.; Pollock, C. J.; Huang, X.; Shao, Y.-T.; Wang, C.; Muller, D. A.; Abruña, H. D.; Yang, P. Operando studies reveal active Cu nanograins for CO_2 electroreduction. *Nature* **2023**, *614*, 262−269.

(3) Masel, R. I.; Liu, Z.; Yang, H.; Kaczur, J. J.; Carrillo, D.; Ren, S.; Salvatore, D.; Berlinguette, C. P. An industrial perspective on catalysts for low-temperature CO_2 electrolysis. *Nat. Nanotechnol.* **2021**, *16*, 118−128.

(4) Birdja, Y. Y.; Pérez-Gallent, E.; Figueiredo, M. C.; Göttle, A. J.; Calle-Vallejo, F.; Koper, M. T. M. Advances and challenges in understanding the electrocatalytic conversion of carbon dioxide to fuels. *Nat. Energy* **2019**, *4*, 732−745.

(5) Shi, G.; Xie, Y.; Du, L.; Fu, X.; Chen, X.; Xie, W.; Lu, T.-B.; Yuan, M.; Wang, M. Constructing Cu−C Bonds in a Graphdiyne-Regulated Cu Single-Atom Electrocatalyst for CO_2 Reduction to CH_4. *Angew. Chem. Int. Ed.* **2022**, *61*, No. e202203569.

(6) Sun, Z.; Ma, T.; Tao, H.; Fan, Q.; Han, B. Fundamentals and Challenges of Electrochemical CO_2 Reduction Using Two-Dimensional Materials. *Chem.* **2017**, *3*, 560−587.

(7) Chang, C.-J.; Lin, S.-C.; Chen, H.-C.; Wang, J.; Zheng, K. J.; Zhu, Y.; Chen, H. M. Dynamic Reoxidation/Reduction-Driven Atomic Interdiffusion for Highly Selective CO_2 Reduction toward Methane. *J. Am. Chem. Soc.* **2020**, *142*, 12119−12132.

(8) Nitopi, S.; Bertheussen, E.; Scott, S. B.; Liu, X.; Engstfeld, A. K.; Horch, S.; Seger, B.; Stephens, I. E. L.; Chan, K.; Hahn, C.; Nørskov, J. K.; Jaramillo, T. F.; Chorkendorff, I. Progress and Perspectives of Electrochemical CO_2 Reduction on Copper in Aqueous Electrolyte. *Chem. Rev.* **2019**, *119*, 7610−7672.

(9) Zhao, J.; Zhang, P.; Yuan, T.; Cheng, D.; Zhen, S.; Gao, H.; Wang, T.; Zhao, Z.-J.; Gong, J. Modulation of $*CH_xO$ Adsorption to Facilitate Electrocatalytic Reduction of CO_2 to CH_4 over Cu-Based Catalysts. *J. Am. Chem. Soc.* **2023**, *145*, 6622−6627.

(10) Zhou, X.; Shan, J.; Chen, L.; Xia, B. Y.; Ling, T.; Duan, J.; Jiao, Y.; Zheng, Y.; Qiao, S.-Z. Stabilizing Cu^{2+} Ions by Solid Solutions to Promote CO_2 Electroreduction to Methane. *J. Am. Chem. Soc.* **2022**, *144*, 2079−2084.

(11) Zhang, Y.; Dong, L.-Z.; Li, S.; Huang, X.; Chang, J.-N.; Wang, J.-H.; Zhou, J.; Li, S.-L.; Lan, Y.-Q. Coordination environment dependent selectivity of single-site-Cu enriched crystalline porous catalysts in CO_2 reduction to CH_4. *Nat. Commun.* **2021**, *12*, 6390.

(12) Guan, A.; Chen, Z.; Quan, Y.; Peng, C.; Wang, Z.; Sham, T.-K.; Yang, C.; Ji, Y.; Qian, L.; Xu, X.; Zheng, G. Boosting CO_2 Electroreduction to CH_4 via Tuning Neighboring Single-Copper Sites. *ACS Energy Lett.* **2020**, *5*, 1044−1053.

(13) Tan, X.; Sun, K.; Zhuang, Z.; Hu, B.; Zhang, Y.; Liu, Q.; He, C.; Xu, Z.; Chen, C.; Xiao, H.; Chen, C. Stabilizing Copper by a Reconstruction-Resistant Atomic Cu−O−Si Interface for Electrochemical CO_2 Reduction. *J. Am. Chem. Soc.* **2023**, *145*, 8656−8664.

(14) Liu, L.; Corma, A. Metal Catalysts for Heterogeneous Catalysis: From Single Atoms to Nanoclusters and Nanoparticles. *Chem. Rev.* **2018**, *118*, 4981−5079.

(15) Wu, Y.; Jiang, Z.; Lu, X.; Liang, Y.; Wang, H. Domino electroreduction of CO_2 to methanol on a molecular catalyst. *Nature* **2019**, *575*, 639−642.

(16) Liu, S.; Li, C.; Zachman, M. J.; Zeng, Y.; Yu, H.; Li, B.; Wang, M.; Braaten, J.; Liu, J.; Meyer, H. M.; Lucero, M.; Kropf, A. J.; Alp, E. E.; Gong, Q.; Shi, Q.; Feng, Z.; Xu, H.; Wang, G.; Myers, D. J.; Xie, J.; Cullen, D. A.; Litster, S.; Wu, G. Atomically dispersed iron sites with a nitrogen−carbon coating as highly active and durable oxygen reduction catalysts for fuel cells. *Nat. Energy* **2022**, *7*, 652−663.

(17) Pan, F.; Yang, X.; O'Carroll, T.; Li, H.; Chen, K.-J.; Wu, G. Carbon Catalysts for Electrochemical CO_2 Reduction toward Multicarbon Products. *Adv. Energy Mater.* **2022**, *12*, 2200586.

(18) Wang, Y.; Wang, D.; Li, Y. Rational Design of Single-Atom Site Electrocatalysts: From Theoretical Understandings to Practical Applications. *Adv. Mater.* **2021**, *33*, 2008151.

(19) Li, Y.; Shan, W.; Zachman, M. J.; Wang, M.; Hwang, S.; Tabassum, H.; Yang, J.; Yang, X.; Karakalos, S.; Feng, Z.; Wang, G.; Wu, G. Atomically Dispersed Dual-Metal Site Catalysts for Enhanced CO_2 Reduction: Mechanistic Insight into Active Site Structures. *Angew. Chem. Int. Ed.* **2022**, *134*, No. e202205632.

(20) Li, Y.; Adli, N. M.; Shan, W.; Wang, M.; Zachman, M. J.; Hwang, S.; Tabassum, H.; Karakalos, S.; Feng, Z.; Wang, G.; Li, Y. C.; Wu, G. Atomically dispersed single Ni site catalysts for high-efficiency CO_2 electroreduction at industrial-level current densities. *Energy Environ. Sci.* **2022**, *15*, 2108−2119.

(21) Li, Z.; Chen, Y.; Ji, S.; Tang, Y.; Chen, W.; Li, A.; Zhao, J.; Xiong, Y.; Wu, Y.; Gong, Y.; Yao, T.; Liu, W.; Zheng, L.; Dong, J.; Wang, Y.; Zhuang, Z.; Xing, W.; He, C.-T.; Peng, C.; Cheong, W.-C.;

Li, Q.; Zhang, M.; Chen, Z.; Fu, N.; Gao, X.; Zhu, W.; Wan, J.; Zhang, J.; Gu, L.; Wei, S.; Hu, P.; Luo, J.; Li, J.; Chen, C.; Peng, Q.; Duan, X.; Huang, Y.; Chen, X.-M.; Wang, D.; Li, Y. Iridium single-atom catalyst on nitrogen-doped carbon for formic acid oxidation synthesized using a general host−guest strategy. *Nat. Chem.* **2020**, *12*, 764−772.
(22) Ji, D.; Fan, L.; Li, L.; Peng, S.; Yu, D.; Song, J.; Ramakrishna, S.; Guo, S. Atomically Transition Metals on Self-Supported Porous Carbon Flake Arrays as Binder-Free Air Cathode for Wearable Zinc−Air Batteries. *Adv. Mater.* **2019**, *31*, 1808267.
(23) Hu, Q.; Han, Z.; Wang, X.; Li, G.; Wang, Z.; Huang, X.; Yang, H.; Ren, X.; Zhang, Q.; Liu, J.; He, C. Facile Synthesis of Sub-Nanometric Copper Clusters by Double Confinement Enables Selective Reduction of Carbon Dioxide to Methane. *Angew. Chem. Int. Ed.* **2020**, *59*, 19054.
(24) Xu, H.; Rebollar, D.; He, H.; Chong, L.; Liu, Y.; Liu, C.; Sun, C.-J.; Li, T.; Muntean, J. V.; Winans, R. E.; Liu, D.-J.; Xu, T. Highly selective electrocatalytic CO_2 reduction to ethanol by metallic clusters dynamically formed from atomically dispersed copper. *Nat. Energy* **2020**, *5*, 623−632.
(25) Karapinar, D.; Huan, N. T.; Ranjbar Sahraie, N.; Li, J.; Wakerley, D.; Touati, N.; Zanna, S.; Taverna, D.; Galvão Tizei, L. H.; Zitolo, A.; Jaouen, F.; Mougel, V.; Fontecave, M. Electroreduction of CO_2 on Single-Site Copper-Nitrogen-Doped Carbon Material: Selective Formation of Ethanol and Reversible Restructuration of the Metal Sites. *Angew. Chem. Int. Ed.* **2019**, *58*, 15098−15103.
(26) Bai, X.; Zhao, X.; Zhang, Y.; Ling, C.; Zhou, Y.; Wang, J.; Liu, Y. Dynamic Stability of Copper Single-Atom Catalysts under Working Conditions. *J. Am. Chem. Soc.* **2022**, *144*, 17140−17148.
(27) Su, X.; Jiang, Z.; Zhou, J.; Liu, H.; Zhou, D.; Shang, H.; Ni, X.; Peng, Z.; Yang, F.; Chen, W.; Qi, Z.; Wang, D.; Wang, Y. Complementary Operando Spectroscopy identification of in-situ generated metastable charge-asymmetry Cu_2-CuN_3 clusters for CO_2 reduction to ethanol. *Nat. Commun.* **2022**, *13*, 1322.
(28) Sun, H.; Chen, L.; Xiong, L.; Feng, K.; Chen, Y.; Zhang, X.; Yuan, X.; Yang, B.; Deng, Z.; Liu, Y.; Rümmeli, M. H.; Zhong, J.; Jiao, Y.; Peng, Y. Promoting ethylene production over a wide potential window on Cu crystallites induced and stabilized via current shock and charge delocalization. *Nat. Commun.* **2021**, *12*, 6823.
(29) Weng, Z.; Wu, Y.; Wang, M.; Jiang, J.; Yang, K.; Huo, S.; Wang, X.-F.; Ma, Q.; Brudvig, G. W.; Batista, V. S.; Liang, Y.; Feng, Z.; Wang, H. Active sites of copper-complex catalytic materials for electrochemical carbon dioxide reduction. *Nat. Commun.* **2018**, *9*, 415.
(30) Zhu, Y.; Yang, X.; Peng, C.; Priest, C.; Mei, Y.; Wu, G. Carbon-Supported Single Metal Site Catalysts for Electrochemical CO_2 Reduction to CO and Beyond. *Small* **2021**, *17*, 2005148.
(31) Pan, F.; Yang, Y. Designing CO_2 Reduction Electrode Materials by Morphology and Interface Engineering. *Energy Environ. Sci.* **2020**, *13*, 2275−2309.
(32) Wu, Z.-Y.; Zhu, P.; Cullen, D. A.; Hu, Y.; Yan, Q.-Q.; Shen, S.-C.; Chen, F.-Y.; Yu, H.; Shakouri, M.; Arregui-Mena, J. D.; Ziabari, A.; Paterson, A. R.; Liang, H.-W.; Wang, H. A general synthesis of single atom catalysts with controllable atomic and mesoporous structures. *Nat. Synth.* **2022**, *1*, 658−667.
(33) García de Arquer, F. P.; Dinh, C.-T.; Ozden, A.; Wicks, J.; McCallum, C.; Kirmani, A. R.; Nam, D.-H.; Gabardo, C.; Seifitokaldani, A.; Wang, X.; Li, Y. C.; Li, F.; Edwards, J.; Richter, L. J.; Thorpe, S. J.; Sinton, D.; Sargent, E. H. CO_2 electrolysis to multicarbon products at activities greater than 1 A cm^{-2}. *Science* **2020**, *367*, 661−666.
(34) Wordsworth, J.; Benedetti, T. M.; Somerville, S. V.; Schuhmann, W.; Tilley, R. D.; Gooding, J. J. The Influence of Nanoconfinement on Electrocatalysis. *Angew. Chem. Int. Ed.* **2022**, *61*, No. e202200755.
(35) Sun, L.; Liu, B. Mesoporous PdN Alloy Nanocubes for Efficient Electrochemical Nitrate Reduction to Ammonia. *Adv. Mater.* **2023**, *35*, 2207305.
(36) Higgins, D.; Hahn, C.; Xiang, C.; Jaramillo, T. F.; Weber, A. Z. Gas-Diffusion Electrodes for Carbon Dioxide Reduction: A New Paradigm. *ACS Energy Lett.* **2019**, *4*, 317−324.
(37) Lees, E. W.; Mowbray, B. A. W.; Parlane, F. G. L.; Berlinguette, C. P. Gas diffusion electrodes and membranes for CO_2 reduction electrolysers. *Nat. Rev. Mater.* **2022**, *7*, 55−64.
(38) Zhou, Z.; Liu, T.; Khan, A. U.; Liu, G. Block copolymer−based porous carbon fibers. *Sci. Adv.* **2019**, *5*, No. eaau6852.
(39) Li, X.; Bi, W.; Chen, M.; Sun, Y.; Ju, H.; Yan, W.; Zhu, J.; Wu, X.; Chu, W.; Wu, C.; Xie, Y. Exclusive Ni−N_4 Sites Realize Near-Unity CO Selectivity for Electrochemical CO_2 Reduction. *J. Am. Chem. Soc.* **2017**, *139*, 14889−14892.
(40) Li, H.; Pan, F.; Qin, C.; Wang, T.; Chen, K.-J. Porous Organic Polymers-Based Single-Atom Catalysts for Sustainable Energy-Related Electrocatalysis. *Adv. Energy Mater.* **2023**, *13*, 2301378.
(41) Peng, L.; Yang, J.; Yang, Y.; Qian, F.; Wang, Q.; Sun-Waterhouse, D.; Shang, L.; Zhang, T.; Waterhouse, G. I. N. Mesopore-Rich Fe−N−C Catalyst with FeN_4−O−NC Single-Atom Sites Delivers Remarkable Oxygen Reduction Reaction Performance in Alkaline Media. *Adv. Mater.* **2022**, *34*, 2202544.
(42) Pan, F.; Li, B.; Sarnello, E.; Fei, Y.; Gang, Y.; Xiang, X.; Du, Z.; Zhang, P.; Wang, G.; Nguyen, H. T.; Li, T.; Hu, Y. H.; Zhou, H.-C.; Li, Y. Atomically Dispersed Iron-Nitrogen Sites on Hierarchically Mesoporous Carbon Nanotubes and Graphene Nanoribbons Networks for CO_2 Reduction. *ACS Nano* **2020**, *14*, 5506−5516.
(43) Funke, H.; Scheinost, A. C.; Chukalina, M. Wavelet analysis of extended x-ray absorption fine structure data. *Phys. Rev. B* **2005**, *71*, No. 094110.
(44) Fei, H.; Dong, J.; Feng, Y.; Allen, C. S.; Wan, C.; Volosskiy, B.; Li, M.; Zhao, Z.; Wang, Y.; Sun, H.; An, P.; Chen, W.; Guo, Z.; Lee, C.; Chen, D.; Shakir, I.; Liu, M.; Hu, T.; Li, Y.; Kirkland, A. I.; Duan, X.; Huang, Y. General synthesis and definitive structural identification of MN_4C_4 single-atom catalysts with tunable electrocatalytic activities. *Nat. Catal.* **2018**, *1*, 63−72.
(45) Yang, J.; Liu, W.; Xu, M.; Liu, X.; Qi, H.; Zhang, L.; Yang, X.; Niu, S.; Zhou, D.; Liu, Y.; Su, Y.; Li, J.-F.; Tian, Z.-Q.; Zhou, W.; Wang, A.; Zhang, T. Dynamic Behavior of Single-Atom Catalysts in Electrocatalysis: Identification of Cu-N_3 as an Active Site for the Oxygen Reduction Reaction. *J. Am. Chem. Soc.* **2021**, *143*, 14530−14539.
(46) Kong, S.; Lv, X.; Wang, X.; Liu, Z.; Li, Z.; Jia, B.; Sun, D.; Yang, C.; Liu, L.; Guan, A.; Wang, J.; Zheng, G.; Huang, F. Delocalization state-induced selective bond breaking for efficient methanol electrosynthesis from CO_2. *Nat. Catal.* **2023**, *6*, 6−15.
(47) Zitolo, A.; Goellner, V.; Armel, V.; Sougrati, M.-T.; Mineva, T.; Stievano, L.; Fonda, E.; Jaouen, F. Identification of catalytic sites for oxygen reduction in iron- and nitrogen-doped graphene materials. *Nat. Mater.* **2015**, *14*, 937−942.
(48) Feaster, J. T.; Shi, C.; Cave, E. R.; Hatsukade, T.; Abram, D. N.; Kuhl, K. P.; Hahn, C.; Nørskov, J. K.; Jaramillo, T. F. Understanding Selectivity for the Electrochemical Reduction of Carbon Dioxide to Formic Acid and Carbon Monoxide on Metal Electrodes. *ACS Catal.* **2017**, *7*, 4822−4827.
(49) Chen, Y.; Fan, Z.; Wang, J.; Ling, C.; Niu, W.; Huang, Z.; Liu, G.; Chen, B.; Lai, Z.; Liu, X.; Li, B.; Zong, Y.; Gu, L.; Wang, J.; Wang, X.; Zhang, H. Ethylene Selectivity in Electrocatalytic CO_2 Reduction on Cu Nanomaterials: A Crystal Phase-Dependent Study. *J. Am. Chem. Soc.* **2020**, *142*, 12760−12766.
(50) Wang, X.; Sun, L.; Reddu, V.; Fisher, A. C. Electrocatalytic Reduction of Carbon Dioxide: Opportunities with Heterogeneous Molecular Catalysts. *Energy Environ. Sci.* **2020**, *13*, 374−403.
(51) Yoon, Y.; Hall, A. S.; Surendranath, Y. Tuning of Silver Catalyst Mesostructure Promotes Selective Carbon Dioxide Conversion into Fuels. *Angew. Chem. Int. Ed.* **2016**, *55*, 15282−15286.
(52) Zhuang, T.-T.; Pang, Y.; Liang, Z.-Q.; Wang, Z.; Li, Y.; Tan, C.-S.; Li, J.; Dinh, C. T.; De Luna, P.; Hsieh, P.-L.; Burdyny, T.; Li, H.-H.; Liu, M.; Wang, Y.; Li, F.; Proppe, A.; Johnston, A.; Nam, D.-H.; Wu, Z.-Y.; Zheng, Y.-R.; Ip, A. H.; Tan, H.; Chen, L.-J.; Yu, S.-H.; Kelley, S. O.; Sinton, D.; Sargent, E. H. Copper nanocavities confine

https://doi.org/10.1021/jacs.3c10524
J. Am. Chem. Soc. 2024, 146, 1423−1434

intermediates for efficient electrosynthesis of C_3 alcohol fuels from carbon monoxide. *Nat. Catal.* **2018**, *1*, 946−951.
(53) Wang, X.; Wang, Z.; García de Arquer, F. P.; Dinh, C.-T.; Ozden, A.; Li, Y. C.; Nam, D.-H.; Li, J.; Liu, Y.-S.; Wicks, J.; Chen, Z.; Chi, M.; Chen, B.; Wang, Y.; Tam, J.; Howe, J. Y.; Proppe, A.; Todorović, P.; Li, F.; Zhuang, T.-T.; Gabardo, C. M.; Kirmani, A. R.; McCallum, C.; Hung, S.-F.; Lum, Y.; Luo, M.; Min, Y.; Xu, A.; O'Brien, C. P.; Stephen, B.; Sun, B.; Ip, A. H.; Richter, L. J.; Kelley, S. O.; Sinton, D.; Sargent, E. H. Efficient electrically powered CO_2-to-ethanol via suppression of deoxygenation. *Nat. Energy* **2020**, *5*, 478−486.
(54) Zhao, Y.; Zhang, X.-G.; Bodappa, N.; Yang, W.-M.; Liang, Q.; Radjenovica, P. M.; Wang, Y.-H.; Zhang, Y.-J.; Dong, J.-C.; Tian, Z.-Q.; Li, J.-F. Elucidating electrochemical CO_2 reduction reaction processes on Cu(hkl) single-crystal surfaces by in situ Raman spectroscopy. *Energy Environ. Sci.* **2022**, *15*, 3968−3977.
(55) Fernández-González, J.; Rumayor, M.; Domínguez-Ramos, A.; Irabien, Á. CO_2 electroreduction: Sustainability analysis of the renewable synthetic natural gas. *Int. J. Greenh. Gas Control* **2022**, *114*, No. 103549.
(56) Wan, X.; Liu, Q.; Liu, J.; Liu, S.; Liu, X.; Zheng, L.; Shang, J.; Yu, R.; Shui, J. Iron atom−cluster interactions increase activity and improve durability in Fe−N−C fuel cells. *Nat. Commun.* **2022**, *13*, 2963.
(57) Lin, X.-M.; Wang, X.-T.; Deng, Y.-L.; Chen, X.; Chen, H.-N.; Radjenovic, P. M.; Zhang, X.-G.; Wang, Y.-H.; Dong, J.-C.; Tian, Z.-Q.; Li, J.-F. In Situ Probe of the Hydrogen Oxidation Reaction Intermediates on PtRu a Bimetallic Catalyst Surface by Core−Shell Nanoparticle-Enhanced Raman Spectroscopy. *Nano Lett.* **2022**, *22*, 5544−5552.
(58) He, M.; Li, C.; Zhang, H.; Chang, X.; Chen, J. G.; Goddard, W. A.; Cheng, M.-j.; Xu, B.; Lu, Q. Oxygen induced promotion of electrochemical reduction of CO_2 via co-electrolysis. *Nat. Commun.* **2020**, *11*, 3844.
(59) Jin, J.; Wicks, J.; Min, Q.; Li, J.; Hu, Y.; Ma, J.; Wang, Y.; Jiang, Z.; Xu, Y.; Lu, R.; Si, G.; Papangelakis, P.; Shakouri, M.; Xiao, Q.; Ou, P.; Wang, X.; Chen, Z.; Zhang, W.; Yu, K.; Song, J.; Jiang, X.; Qiu, P.; Lou, Y.; Wu, D.; Mao, Y.; Ozden, A.; Wang, C.; Xia, B. Y.; Hu, X.; Dravid, V. P.; Yiu, Y.-M.; Sham, T.-K.; Wang, Z.; Sinton, D.; Mai, L.; Sargent, E. H.; Pang, Y. Constrained C_2 adsorbate orientation enables CO-to-acetate electroreduction. *Nature* **2023**, *617*, 724−729.
(60) Zeng, Y.; Zhao, J.; Wang, S.; Ren, X.; Tan, Y.; Lu, Y.-R.; Xi, S.; Wang, J.; Jaouen, F.; Li, X.; Huang, Y.; Zhang, T.; Liu, B. Unraveling the Electronic Structure and Dynamics of the Atomically Dispersed Iron Sites in Electrochemical CO_2 Reduction. *J. Am. Chem. Soc.* **2023**, *145*, 15600−15610.
(61) Yang, Y.; Fu, J.; Ouyang, Y.; Tang, T.; Zhang, Y.; Zheng, L.-R.; Zhang, Q.-H.; Liu, X.-Z.; Wang, J.; Hu, J.-S. In-situ constructed Cu/CuNC interfaces for low-overpotential reduction of CO_2 to ethanol. *Nat. Sci. Rev.* **2022**, *10*, nwac248.
(62) Chang, Q.; Liu, Y.; Lee, J.-H.; Ologunagba, D.; Hwang, S.; Xie, Z.; Kattel, S.; Lee, J. H.; Chen, J. G. Metal-Coordinated Phthalocyanines as Platform Molecules for Understanding Isolated Metal Sites in the Electrochemical Reduction of CO_2. *J. Am. Chem. Soc.* **2022**, *144*, 16131−16138.
(63) Wang, Y.; Li, B.; Xue, B.; Libretto, N.; Xie, Z.; Shen, H.; Wang, C.; Raciti, D.; Marinkovic, N.; Zong, H.; Xie, W.; Li, Z.; Zhou, G.; Vitek, J.; Chen, J. G.; Miller, J.; Wang, G.; Wang, C. CO electroreduction on single-atom copper. *Sci. Adv.* **2023**, *9*, No. eade3557.
(64) Cai, Y.; Fu, J.; Zhou, Y.; Chang, Y.-C.; Min, Q.; Zhu, J.-J.; Lin, Y.; Zhu, W. Insights on forming N,O-coordinated Cu single-atom catalysts for electrochemical reduction CO_2 to methane. *Nat. Commun.* **2021**, *12*, 586.
(65) Yang, J.; Qi, H.; Li, A.; Liu, X.; Yang, X.; Zhang, S.; Zhao, Q.; Jiang, Q.; Su, Y.; Zhang, L.; Li, J.-F.; Tian, Z.-Q.; Liu, W.; Wang, A.; Zhang, T. Potential-Driven Restructuring of Cu Single Atoms to Nanoparticles for Boosting the Electrochemical Reduction of Nitrate to Ammonia. *J. Am. Chem. Soc.* **2022**, *144*, 12062−12071.
(66) Xiong, L.; Zhang, X.; Chen, L.; Deng, Z.; Han, S.; Chen, Y.; Zhong, J.; Sun, H.; Lian, Y.; Yang, B.; Yuan, X.; Yu, H.; Liu, Y.; Yang, X.; Guo, J.; Rümmeli, M. H.; Jiao, Y.; Peng, Y. Geometric Modulation of Local CO Flux in Ag@Cu_2O Nanoreactors for Steering the CO_2RR Pathway toward High-Efficacy Methane Production. *Adv. Mater.* **2021**, *33*, 2101741.
(67) Wang, X.; Ou, P.; Wicks, J.; Xie, Y.; Wang, Y.; Li, J.; Tam, J.; Ren, D.; Howe, J. Y.; Wang, Z.; Ozden, A.; Finfrock, Y. Z.; Xu, Y.; Li, Y.; Rasouli, A. S.; Bertens, K.; Ip, A. H.; Graetzel, M.; Sinton, D.; Sargent, E. H. Gold-in-copper at low *CO coverage enables efficient electromethanation of CO_2. *Nat. Commun.* **2021**, *12*, 3387.
(68) Lin, L.; Liu, T.; Xiao, J.; Li, H.; Wei, P.; Gao, D.; Nan, B.; Si, R.; Wang, G.; Bao, X. Enhancing CO_2 Electroreduction to Methane with a Cobalt Phthalocyanine and Zinc−Nitrogen−Carbon Tandem Catalyst. *Angew. Chem. Int. Ed.* **2020**, *59*, 22408−22413.
(69) Heng, J.-M.; Zhu, H.-L.; Zhao, Z.-H.; Yu, C.; Liao, P.-Q.; Chen, X.-M. Dicopper(I) Sites Confined in a Single Metal−Organic Layer Boosting the Electroreduction of CO_2 to CH_4 in a Neutral Electrolyte. *J. Am. Chem. Soc.* **2023**, *145*, 21672−21678.
(70) Wang, H.; Tzeng, Y.-K.; Ji, Y.; Li, Y.; Li, J.; Zheng, X.; Yang, A.; Liu, Y.; Gong, Y.; Cai, L.; Li, Y.; Zhang, X.; Chen, W.; Liu, B.; Lu, H.; Melosh, N. A.; Shen, Z.-X.; Chan, K.; Tan, T.; Chu, S.; Cui, Y. Synergistic enhancement of electrocatalytic CO_2 reduction to C_2 oxygenates at nitrogen-doped nanodiamonds/Cu interface. *Nat. Nanotechnol.* **2020**, *15*, 131−137.
(71) Wang, X.; de Araújo, J. F.; Ju, W.; Bagger, A.; Schmies, H.; Kühl, S.; Rossmeisl, J.; Strasser, P. Mechanistic reaction pathways of enhanced ethylene yields during electroreduction of CO_2−CO co-feeds on Cu and Cu-tandem electrocatalysts. *Nat. Nanotechnol.* **2019**, *14*, 1−8.
(72) Jouny, M.; Luc, W.; Jiao, F. High-rate electroreduction of carbon monoxide to multi-carbon products. *Nat. Catal.* **2018**, *1*, 748−755.

https://doi.org/10.1021/jacs.3c10524
J. Am. Chem. Soc. 2024, 146, 1423−1434